In situ Observations of Whistler-mode Chorus Waves Guided by Density Ducts

Rui Chen[1,2], Xinliang Gao[1,2]*, Quanming Lu[1,2+], Lunjin Chen[3], Bruce T. Tsurutani[4], Wen Li[5], Binbin Ni[2,6] and Shui Wang[1,2]

[1]CAS Key Lab of Geospace Environment, School of Earth and Space Sciences, University of Science and Technology of China, Hefei, China

[2]CAS Center for Excellence in Comparative Planetology, Hefei, China

[3]Department of Physics, University of Texas at Dallas, Richardson, TX, USA

[4]Retired, Pasadena, CA, USA

[5]Center for Space Physics, Boston University, Boston, MA, USA

[6]Department of Space Physics, School of Electronic Information, Wuhan University, Wuhan, China

Corresponding Author: Xinliang Gao, Email:*gaoxl@mail.ustc.edu.cn

Abstract

In this paper, we report the proof of the existence of density ducts in the Earth's magnetosphere by studying in situ observations of whistler-mode chorus waves using NASA's Van Allen Probe-A data. Chorus waves, originally excited inside the density ducts with wave normal angles (WNAs) smaller than the Gendrin angle at near equator region, are efficiently confined to a limited area inside density ducts (i.e., ducted regions), and remain with small WNAs as they propagate towards high latitudes. The ducted region becomes narrower for the higher-frequency waves. Chorus waves with WNAs larger than the Gendrin angle are not guided by density ducts. Our study reveals that density ducts can effectively control the property and distribution of chorus waves, and may ultimately regulate electron dynamics in the Earth's or other planetary radiation belts.

1. Introduction

Whistler-mode chorus waves are intense and naturally generated electromagnetic emissions observed frequently in the near-Earth space (Tsurutani and Smith, 1974; Horne et al., 2005; Thorne et al., 2010, 2013; Gao et al., 2014; An et al., 2019) and other magnetized planets (Scarf et al., 1979; Gurnett et al., 1981, 1986; Shprits et al., 2018). It has been well recognized that these waves play a pivotal role in the dynamics of planetary radiation belts (Kennel and Petschek, 1966; Horne et al., 2005; Thorne et al., 2010, 2013; Reeves et al., 2013; Mozer et al., 2014), a zone of high-energy electrons that are trapped by the intrinsic magnetic fields. Satellite observations have shown that density ducts with cross-field plasma density enhancements (or depletions) possibly exist frequently in the Earth's radiation belts (Smith et al., 1968; Angerami, 1970; Koons 1989; Sonwalker et al., 1994; Moullard et al., 2002; Sonwalker, 2006; Bell et al., 2009; Li et al., 2011; Loi et al., 2015). The existence of these ducts can change the global distribution and properties of chorus waves, and thus significantly affects the dynamics of high-energy electrons in the radiation belt.

The possible guidance of whistler-mode waves in density ducts has drawn attention for over five decades (Smith et al., 1960, 1968; Scarabucci and Smith, 1971; Karpman and Kaufman, 1982; Koons 1989; Moullard et al., 2002; Bell et al., 2009; Li et al., 2011). A number of theoretical (Smith et al., 1960; Scarabucci and Smith, 1971; Karpman and Kaufman, 1982) and simulation studies (Streltsov et al., 2006, 2007; Woodroffe et al., 2013; Streltsov and Bengtson, 2020) have demonstrated that whistler-mode waves can be spatially confined in a duct when its transverse scale size is comparable to or smaller than the perpendicular wavelength of the waves. However, in situ evidence for such a concept is still absent, because of incomplete measurements of electromagnetic fields (only one or two dimensions, Bryant et al., 1985; Cornilleau-Wehrlin et al., 1997) and reliable plasma density measurements (uncertainty within a factor of ~2, Li et al., 2010). As a result, previous observations only revealed the correlation between density variation and chorus wave occurrence (Koons 1989; Moullard et al., 2002; Li et al., 2011).

To thoroughly investigate chorus waves guided by density ducts, we have acquired the simultaneous measurements of high-resolution three-dimensional electromagnetic fields—to obtain the full polarization properties of chorus waves, and sufficiently accurate plasma densities—to identify the density ducts, both using NASA’s Van Allen Probes mission instrumentation (Kletzing et al., 2013; Wygant et al., 2013; Spence et al., 2013). Based on the data, we will conduct theoretical wave propagation calculations. Here we analyze in detail the trapping of whistler-mode chorus waves by density ducts with cross-field density enhancements, and perform a quantitative comparison with the existing wave propagation theory. As shown below, chorus waves, originating from nearby sources, display significantly different properties inside and outside density ducts.

2. Data

Van Allen probes, previously called the “Radiation Belt Storm Probes” (RBSP) mission, are twin spin-stabilized spacecraft (A and B) operating in near-equatorial, highly elliptical, and low-inclination orbits with perigees of $\sim 1.1R_E$ and apogees of $\sim 5.8R_E$. The instruments onboard the satellites provide accurate in situ measurements of wave environment and particle fluxes in the Earth's inner magnetosphere. The Electric and Magnetic Field Instrument Suite and Integrated Science (EMFISIS) suite (Kletzing et al., 2013) onboard two probes provide high time-resolution electromagnetic fields (~35,000 S/sec), low-resolution dc magnetic fields (64 S/sec), and high-frequency power spectra (1/6 S/sec). The low-resolution dc magnetic fields are treated as the background magnetic field, while the high-resolution wave magnetic fields are analyzed to obtain polarization information (such as the wave normal angle and pointing flux) of chorus waves followed Means' method (Means, 1972). The background plasma density is estimated by the upper-hybrid wave band (Kurth et al., 2015) shown in the high-frequency power spectra, or inferred from the spacecraft potential (Wygant et al., 2013). The Energetic Particle, Composition and Thermal Plasma Suite (ECT, Spence et al., 2013) consists of the Helium Oxygen Proton Electron (HOPE) Mass Spectrometer (Funsten et al., 2013), the Magnetic Electron Ion Spectrometer (MagEIS, Blake et al., 2013), and the Relativistic Electron Proton Telescope (REPT, Baker et al., 2013). The three instruments collectively cover the electron and ion spectra from eV to tens of MeV.

3. Observation Results

We report RBSP-A spacecraft measurements during 06:10-06:35 UT on January 30, 2014. The spacecraft was in the inner magnetosphere at a magnetic latitude of -18.8° and a radial distance of ~5.7 Earth radii (Fig. 1a), when it encountered two density ducts at about 06:23 and 06:28 UT, characterized by a density increase up to a factor of two (Fig. 1c). The density shown in Fig. 1c is obtained from two different techniques: (1) inferred from the upper-hybrid frequency f_{uh} shown in Fig. 1b (red line), and (2) inferred from the spacecraft potential (black line). The remarkable consistency between the two measurements demonstrates a high reliability of the presence of density ducts. Angerami (1970) revealed that the width of ducts (in L-shell direction) ranges between 0.035 and 0.07 earth radii, about ~200-450km at equator. Sonwalkar et al. (1994) also estimated the width as ~367km at the equator. Here the cross-field scale of two density ducts is estimated to be ~460 km based on the spacecraft velocity (~2.56 km/s). The width is ~280km in radial direction, and ~350km in azimuthal direction, which is similar to previous results.

In Figs. 1d and 1e, there are intense electromagnetic waves in the whistler-mode frequency range, i.e., with frequencies $0.1f_{ce} < f < 0.5f_{ce}$, both inside and outside the density ducts. Here f_{ce} represents the equatorial electron cyclotron frequency. These whistler-mode waves, also called as chorus waves, are captured by RBSP-A as they propagate southward from their source region (i.e., the magnetic equator), which is inferred from the anti-parallel orientation ($\theta_{poyn} = 180^{\circ}$) of the wave Poynting vector with respect to the background magnetic field (Fig. 1f). It is generally accepted that chorus waves are generated from the anisotropic energetic electron population (from ~10 to 100 keV) at the magnetic equator with small wave normal angles (WNA$\leq 20^{\circ}$, Gary et al., 2000; Omura et al., 2008; Lu et al., 2019), and the wave propagation becomes more and more oblique as they propagate in the Earth's dipole magnetic field (Agapitov et al., 2013; Chen et al., 2013; Lu et al., 2019). As shown in Fig. 1g all chorus waves outside the density ducts have quite large WNAs ($\geq \sim 60^{\circ}$) at the observation site, which is consistent with previous theoretical ray tracing and full kinetic simulation results (Chen et al., 2013; Lu et al., 2013). However, chorus waves inside the density ducts exhibit distinctly different properties compared with waves outside. The whistler-mode spectra inside the density ducts are found to have much lower frequency values, which even reach down to ~$0.20 f_{ce}$ (Fig. 1d). In addition, chorus waves below ~1500 Hz still have very small WNAs (Fig. 1g), i.e., only ~20°, even at such a relatively high magnetic latitudes (-18.8°). More interestingly, the chorus WNAs exhibit a frequency-dependence inside each density duct: chorus waves with higher frequencies only contain small WNAs over narrower regions (Fig. 1g), while the waves above ~1700 Hz are highly oblique, similar to those outside the density ducts (Fig. 1g).

This chorus event provides in situ evidence of whistler-mode chorus waves guided by density ducts. In the remainder of this article, we will demonstrate the details of this event can be well explained by the existing theories of whistler mode wave ducting.

During the interval of interest, RBSP-A also recorded several high time-resolution (~30 micro second) burst segments of electric and magnetic field vectors, and we conduct a polarization analysis for each burst segment by using the Means' method (Means, 1972). Two examples are provided in Fig. 2: one is inside the density duct, and the other is outside the density duct, which also have been marked by red arrows in the bottom of Figure 1. Whistler-mode chorus waves in the Earth's magnetosphere typically have discrete fine structures, such as rising tones shown in Fig. 2a. The spectra in event I can be considered as the superposition of two remarkably different groups of chorus waves according to their frequencies and WNAs. In one group, chorus waves have properties closely resembling those outside the density duct (i.e., event II), whose magnetic power peaks at about 1800 Hz (Fig. 2a) and WNAs are mainly larger than 60° (Fig. 2b). In the other wave group, there are only quasi-parallel chorus waves with WNAs smaller than 30° (Fig. 2b), and their power peaks at about 1300 Hz (Fig. 2a).

It is reasonable to assume that chorus waves inside and outside the ducts come from nearby wave generation sources at the magnetic equator, supported by their very close locations and the same southward propagating direction of the waves (Figs. 1f and 2c). The energetic electrons that presumably drive the generation of the two regions almost have the same velocity distribution as shown in the RBSP observations (Figs. 3a and 3b), which could be fitted into a multi-component bi-Maxwellian as $f = \sum_i f_i$, where

$$f_i = n_i \sqrt{\frac{m}{2\pi T_{\parallel i}}} \frac{m}{2\pi T_{\perp i}} exp\left(-\frac{mv_{\parallel}^2}{2T_{\parallel i}} - \frac{mv_{\perp}^2}{2T_{\perp i}}\right),$$

here $v_{\parallel}$ and $v_{\perp}$ are the parallel and perpendicular velocities with respect to the background magnetic field. $T_{\parallel i}$ and $T_{\perp i}$ are the parallel and perpendicular temperatures of the component i. The number density of each component is represented by n_i. All the parameters are presented in Table 1. The cold ($T_{\parallel c}$, $T_{\perp c} = 5eV$) electron density n_c inside the duct (18.7 cm^{-3}) is about twice as large as the value outside the duct ($9.6cm^{-3}$). Other fitting parameters are same for two distributions, since there is little difference between them. The warm electron distribution is fitted by summing three components (i.e., *i*=3): $n_w = 0.52cm^{-3}$, $T_{\parallel w} = 52.4eV$ and $T_{\perp w}/T_{\parallel w} = 1.32$; $n_{h1} = 0.044cm^{-3}$, $T_{\parallel h1} = 2.42keV$ and $T_{\perp h1}/T_{\parallel h1} = 1.42$; $n_{h2} = 0.0027cm^{-3}$, $T_{\parallel h2} = 12.42keV$ and $T_{\perp h2}/T_{\parallel h2} = 1.37$.

Since chorus waves are typically generated from anisotropic electrons at the magnetic equator (Gary et al., 2000; Omura et al., 2008; Lu et al., 2019), we need to transform the fitted local distribution into the equatorial electron distribution. The method employed in this study is the same as that in Summers et al. (2012), which is based on Liouville's theorem that the distribution function is preserved along the field line, with the conservation of the first adiabatic invariant (i.e., magnetic moment) and the particle total kinetic energy. The equatorial distribution parameters derived are: $n_w = 0.63cm^{-3}$, $T_{\parallel w} = 52.4eV$ and $T_{\perp w}/T_{\parallel w} = 1.62$; $n_{h1} = 0.059cm^{-3}$, $T_{\parallel h1} = 2.42keV$ and $T_{\perp h1}/T_{\parallel h1} = 1.89$; $n_{h2} = 0.0035cm^{-3}$, $T_{\parallel h2} = 12.42keV$ and $T_{\perp h2}/T_{\parallel h2} = 1.76$. The equatorial background magnetic field B_{eq} are 164.8nT (inside) and 167.9nT (outside), estimated using a simple dipole field. It is worth noting that this event is captured during a very quiet period (dynamic pressure < 1.0nPa, SYM-H index around ~-15nT, and AE index < 60nT), so the simple dipole field is used in this study. Table 2 gives the parameters of equatorial electron distribution in the same format as Table 1.

With a widely used linear model, such as BO (Xie, 2019), we find the electron density will modulate the frequencies of unstable whistler mode waves. Figs. 3c and

3d illustrate the dispersion relation of unstable whistler modes for both events obtained from the linear model by input equatorial distribution parameters. Linear theoretical results indicate that the unstable whistler waves inside the duct tend to have lower frequencies (Fig. 3c). Outside the duct, the frequency of most unstable whistler mode waves is about 0.36 f_{ce} (~1700 Hz; Fig. 3d), while the one inside the duct decreases to 0.30 f_{ce} (~1400 Hz; Fig. 3c).

To understand the behavior of whistler-mode chorus waves inside the density duct, we employ the theoretical model developed by Streltsov et al. (2006) with the quasi-longitudinal approximation given by

$$\frac{f_{ce}^2}{f^2} sin^2\theta \ll 2 \left|1 - \frac{f_{pe}^2}{f^2}\right| cos\theta, (1)$$

where f is the frequency of whistler-mode wave, and f_{ce} and f_{pe} are the electron gyrofrequency and plasma frequency, respectively. We confirm that the quasi-longitudinal approximation is valid for all whistler-mode chorus waves during the interval of interest in Fig. 1. For simplicity, the duct is treated as a symmetric density hump across the background magnetic field but kept constant along the field line. Since the spatial scale of density duct is only ~400 km, the background magnetic field is nearly uniform inside the density duct. Then the ducted whistler-mode waves should follow the quasi-longitudinal dispersion relation written as:

$$k^2 - \frac{f_{ce}}{f} k_{\parallel} k + \frac{4\pi^2 f_{pe}^2}{c^2} = 0, \ (2)$$

where k is the magnitude of the wave vector which has perpendicular and parallel components $k_{\perp}$ and $k_{\parallel}$ (defined relative to the background magnetic field), and c is the light speed. We focus on a specific wave mode with frequency f, which remains unchanged during the propagation. A good approximation for the strong inhomogeneity across the magnetic field line leads to an almost constant $k_{||}$ during quasi-parallel propagation. Finally, we obtain a formula describing how $k_{\perp}$, essentially equivalent to the WNA, depends on the electron density n_e:

$$n_e = \frac{m_e}{\mu_0 e^2}\left(-k_{\perp}^2 + \frac{f_{ce}}{f}k_{\parallel}\sqrt{k_{\perp}^2 + k_{\parallel}^2} - k_{\parallel}^2\right). \quad (3)$$

Here, m_e, e, μ_0 are the electron mass, electron charge, and vacuum permeability, respectively. Taking a 1100-Hz whistler mode wave as an example, we calculate its $k_{\parallel}$ according to Eq. (2) with the local electron density n_e (~19.26cm^{-3}) and the power-weighted WNA (~27.8°) extracted from event I in Fig. 2. Then, based on Eq. (3), we can plot the blue curve for the 1100-Hz whistler mode wave with the fixed f and $k_{\parallel}$ in Fig. 4b.

For each curve, there are two critical densities: $n_0 = \frac{m_e k_{\parallel}^2}{\mu_0 e^2}\left(\frac{f_{ce}}{f} - 1\right)$ with $k_{\perp} = 0$ and $n_1 = \frac{m_e k_{\parallel}^2}{\mu_0 e^2}\left(\frac{f_{ce}}{2f}\right)^2$ with $k_{\perp} = k_{\perp}^*$. Here, $k_{\perp}^*$ corresponds to the Gendrin angle ($arccos\frac{2f}{f_{ce}}$, Gendrin, 1961). The electron density inside the duct peaks at n_{in} (~19.4 cm^{-3} for the first duct), and decreases to the ambient density n_{out} (~10 cm^{-3}). It is found that these densities satisfy $n_{out} < n_0 < n_{in} < n_1$ for all lower-band (<~2500 Hz) whistler waves. Inside the duct, if the whistler wave has a small $k_{\perp} < k_{\perp}^*$, i.e., quasi-parallel propagating wave, then its $k_{\perp}$ continues to decline along the curve while propagating outward (Fig. 4b). However, when the perpendicular wave number $k_{\perp}$ falls to zero, this whistler mode cannot propagate outward since there is no real solution of $k_{\perp}$ below n_0 (Fig. 4b), but the wave will be reflected toward the center of the duct. Therefore, this whistler mode wave will be confined within the region where the electron density n_e is between n_0 and n_{in} (i.e., ducted region), but it can still propagate along the field line and remain in quasi-parallel propagation. This is why lower-frequency (<1500 Hz) chorus waves inside density ducts still have very small WNAs after they reach the higher-latitude region (~18.8°) as displayed in Figs. 1 and 2.

However, in the case of an oblique whistler wave (i.e., $k_\perp > k_\perp^*$), the curve smoothly extends to low densities (n_{out}) with increasing $k_\perp$ (Fig. 4b), meaning oblique whistler wave will not be confined by the density duct. Therefore, oblique whistler waves with WNAs larger than Gendrin angle can freely propagate inside or outside density ducts. Here we conclude that oblique chorus waves detected inside the duct (Figs. 1d and 2a) are originally excited by outside sources, and then propagate into the duct after they become sufficiently oblique at high latitudes. This is supported by the following arguments. Whistler waves excited inside the duct must be below ~2300 Hz (or $0.5f_{ce}$; Fig. 3c), so they should be confined inside the duct with small WNAs as predicted in Fig. 4b. On the other hand, both the magnetic power and frequencies of obliquely propagating chorus waves are nearly the same as those of waves detected outside the duct (Figs. 1d and 2a), which can be well described by the linear results given in Fig. 3d (outside) rather than Fig. 3c (inside).

Fig. 4a exhibits an expanded view of the shaded region in panel b. As was noted in panel b, a whistler wave with the frequency f (<~2300 Hz) will be confined within the ducted region where $n_0 < n_e < n_{in}$. In Fig. 4a, we further find the critical density n_0 is positively correlated with the wave frequency f, i.e., the n_0 for

800-Hz, 900-Hz, 1000-Hz, and 1100-Hz whistler modes is about 17.32, 17.36, 17.40, and 17.44 cm^{-3}, respectively. Therefore, a whistler mode wave with a lower frequency can propagate further away from the center of the duct, meaning the ducted region of whistler mode is expected to become relatively wider with lower wave f, which has been observed in Fig. 1g. Figs. 5a-5d illustrate the magnetic amplitudes of 800-Hz, 900-Hz, 1000-Hz, and 1100-Hz whistler waves as a function of time, which can also be considered as the spatial distribution of wave amplitudes since the density duct can be assumed to be a statistic structure during this short interval. For each whistler mode wave frequency, we calculate its magnetic amplitude by integrating magnetic power from both wave spectrum data ($B_{w,s}$; Fig. 1d) and burst segments ($B_{w,b}$; Fig. 2a) recorded during this interval, denoted by line and dots, respectively. Although $B_{w,b}$ is larger than $B_{w,s}$ occasionally during some intervals, the trend of variation is very consistent (Figs. 5a-5d). The ducted region for each wave is then determined to be the region where the magnetic amplitude is larger than the background (or outside) value. This has been shaded in gray in each panel. For 800-Hz to 1100-Hz whistler waves, the ducted region is estimated as 125, 106, 82, and 61 km, respectively, corresponding to $n_0^* =$ 17.63, 18.09, 18.52, 18.71cm^{-3}. As a reference, we plot the first density duct in each panel, and mark the theoretical n_0 for these four wave modes. It is important to note that there is a clear trend that the ducted region becomes narrower with the increasing wave frequency (Figs. 5a-5d).

4. Summary and Discussion

In this paper, we report the in situ observation of whistler-mode chorus waves guided by density ducts with small-scale density enhancements. We find chorus waves, originally excited inside ducts with WNAs smaller than the Gendrin angle at near equator region, are efficiently confined within the density ducts, and remain with small WNAs when they propagating towards high latitudes as predicted by theory. In contrast, chorus waves from an outside source become very oblique (i.e., WNAs larger than the Gendrin angle) during their propagation away from the equator, and then they can freely penetrate into (and out of) density ducts. Although there have been some previous observations showing the correlation between density variations and chorus wave occurrence (mith et al., 1968; Angerami, 1970; Koons 1989; Sonwalker et al., 1994; Moullard et al., 2002; Sonwalker, 2006; Bell et al., 2009; Li et al., 2011; Loi et al., 2015), we believe our study can provide significant evidence for the existence of density ducts in the Earth's magnetosphere.

Our analyses find that there are still some deviations between theoretical n_0 and observed n_0^* - specifically, the observed n_0^* is always larger than the theoretical one. From 800 Hz to 1100 Hz, the deviation δn $(= n_0^* - n_0)$ increases from $0.31 cm^{-3}$ to $1.27 cm^{-3}$, which becomes very significant for higher-frequency chorus waves. We speculate that the deviation is mainly caused by the damping effect during the wave propagation, which has not yet been taken into consideration in existing theories. Recent observations (Min et al., 2014; Artemyev and Mourenas, 2020) and simulations (Gary et al., 2011) have revealed that chorus waves with finite wave normal angles can accelerate electrons through Landau resonance during the propagation. That is, chorus waves will experience a certain level of damping even inside the density duct, leading to a narrower ducted region compared with the present theoretical one. Since whistler waves with a higher frequency tend to have a relatively stronger parallel electric field and experience stronger Landau damping (Verkhoglyadova et al., 2010; Gao et al., 2016), the deviation δn for higher-frequency wave becomes more significant. Therefore, the spatial scale of the ducted regions should be controlled by both the ducting and damping effects.

Chorus waves are Earth's own "cyclotron accelerator" that accelerates radiation belt electrons (Horne et al., 2005; Thorne et al., 2013; Reeves et al., 2013; Mozer et al., 2014), and their distribution and properties can be effectively regulated by density ducts. Satellite observations have shown that density ducts with cross-field plasma density enhancements or depletions exist ubiquitously in space (Koons 1989; Moullard et al., 2002; Li et al., 2011). Therefore, we suggest that density ducts may play an important role in modulating energetic electron dynamics in the Earth's or other planetary radiation belts.

Recently, Streltsov and Bengtson (2020) also reported the localized packages of whistler waves trapped inside high-density ducts, and estimated the range of wavelengths that can be trapped by density ducts based on the measurement and ducting theory (Streltsov et al., 2006, 2007). In this study, we report a peculiar chorus event (at far away from the magnetic equator, i.e., MLAT = ~-18.8°), in which lower-band chorus waves inside and outside the density ducts are simultaneously observed. Based on the dispersion relation obtained from the linear model and ducting theory, we confirm that the quasi-parallel chorus waves can be efficiently confined within the density ducts, but the oblique chorus waves can freely penetrate into the density duct. Our study not only presents a clear comparison of chorus waves between ducted (inside) and non-ducted (outside) by density ducts, but also provide significant evidence for wave ducting. Note that the ideal direct evidence of wave ducting requires the joint observation by two or more probes at distant latitudes along one field line, which is too difficult to satisfy with existing data. In this study, based on the Van Allen Probe data, we have conducted a quantitatively comparison between the ducting theory and observations, which well supports the ducting effects of the density enhancement. Although not ideal direct evidence, our results still provide the significant observational support.

References

Agapitov, O., Artemyev, A., Krasnoselskikh, V., Khotyaintsev, Y. V., Mourenas, D., Breuillard, H., Balikhin, M., & Rolland, G. (2013). Statistics of whistler-mode waves in the outer radiation belt: Cluster STAFF-SA measurements, Journal of Geophysical Research: Space Physics, 118, 3407–3420. https://doi.org/10.1002/jgra.50312

Angerami, J. J. (1970). Whistler duct properties deduced from VLF observations made with the OGO 3 satellite near the magnetic equator, Journal of Geophysical Research, 75, 6115. https://doi.org/10.1029/JA075i031p06115

An, X., Li, J., Bortnik, J., Decyk, V., Kletzing, C., & Hospodarsky, G. (2019). Unified View of Nonlinear Wave Structures Associated with Whistler-Mode Chorus, Physical Review Letters, 122, 045101.

https://doi.org/10.1103/PhysRevLett.122.045101

Artemyev, A. V., & Mourenas, D. (2020). On whistler mode wave relation to electron field-aligned plateau populations. Journal of Geophysical Research: Space Physics, 125, e2019JA027735. https://doi.org/10.1029/2019JA027735

Baker, D. N., Kanekal, S. G., Hoxie, V. C., Batiste, S., Bolton, M., Li, X., et al. (2013). The Relativistic Electron-Proton Telescope (REPT) instrument on board the Radiation Belt Storm Probes (RBSP) spacecraft: Characterization of Earth's radiation belt high-energy particle populations. Space Science Reviews, 179, 337–381. https://doi.org/10.1007/s11214-012-9950-9

Bell, T. F., U. S. Inan, N. Haque, and J. S. Pickett (2009), Source regions of banded chorus, Geophys. Res. Lett., 36, L11101. https://doi.org/10.1029/2009GL037629

Blake, J. B., Carranza, P. A., Claudepierre, S. G., Clemmons, J. H., Crain, W. R., Dotan, Y., et al. (2013). The magnetic electron ion spectrometer (MagEIS) instruments aboard the Radiation Belt Storm Probes (RBSP) spacecraft. Space Science Reviews, 179, 383–421. https://doi.org/10.1007/ s11214-013-9991-8

Bryant, D. A., Krimigis, S. M., & Haerendel, G. (1985). Outline of the Active Magnetospheric Particle Tracer Explorers (AMPTE) Mission. IEEE Transactions on Geoscience and Remote Sensing, GE-23, 177. https://doi.org/10.1109/TGRS.1985.289511

Chen, L., Thorne, R. M., Li, W., & Bortnik, J. (2013). Modeling the wave normal distribution of chorus waves. Journal of Geophysical Research: Space Physics, 118, 1074–1088. https://doi.org/10.1029/2012JA018343

Cornilleau-Wehrlin, N., et al. (1997), The cluster spatio-temporal analysis of field fluctuations (staff) experiment, Space Science Reviews, 79, 107–136. https://doi.org/10.1023/A:1004979209565

Funsten, H. O., Skoug, R. M., Guthrie, A. A., MacDonald, E. A., Baldonado, J. R., Harper, R. W., et al. (2013). Helium, Oxygen, Proton, and Electron (HOPE) mass spectrometer for the Radiation Belt Storm Probes mission. Space Science Reviews, 179, 423–484. https://doi.org/10.1007/ s11214-013-9968-7

Gao, X., Li, W., Thorne, R. M., Bortnik, J., Angelopoulos, V., Lu, Q., Tao, X., & Wang, S. (2014). New evidence for generation mechanisms of discrete and hiss-like whistler mode waves. Geophysical Research Letters, 41, 4805–4811. https://doi.org/10.1002/2014GL060707

Gao, X., Lu, Q., Bortnik, J., Li, W., Chen, L., & Wang, S. (2016). Generation of multiband chorus by lower band cascade in the Earth’s magnetosphere. Geophysical Research Letters, 43, 2343–2350. https://doi.org/10.1002/2016GL068313

Gary, S. P., Liu, K., & Winske, D. (2011). Whistler anisotropy instability at low electron β: Particle-in-cell simulations. Physics of Plasmas, 18, 082902. https://doi.org/10.1063/1.3610378

Gary, S. P., Winske, D., & Hesse, M. (2000). Electron temperature anisotropy instabilities: Computer simulations. Journal of Geophysical Research, 105, 10,751-10,759. https://doi.org/10.1029/1999JA000322

Gendrin, R. (1961). Le guidage des whistlers par le champ magnetique. Planetary and

Space Science, 5, 274-282. https://doi.org/10.1016/0032-0633(61)90096-4

Gurnett, D. A., Kurth, W. S., & Scarf, F. L. (1981). Plasma Waves Near Saturn: Initial Results from Voyager 1. Science, 212, 235-239. https://doi.org/10.1126/science.212.4491.235

Gurnett, D. A., Kurth, W. S., Scarf, F. L., & Poynter, R. L. (1986). First Plasma Wave Observations at Uranus. Science, 233, 106-109. https://doi.org/10.1126/science.233.4759.106

Horne, R. B., Thorne, R. M., Shprits, Y. Y., Meredith, N. P., Glauert, S. A., Smith, A. J., & Decreau, P. M. E. (2005). Wave acceleration of electrons in the Van Allen radiation belts. Nature, 437, 227–230. https://doi.org/10.1038/nature03939

Karpman, V. I., & Kaufman, R. N. (1982). Whistler wave propagation in density ducts. Journal of Plasma Physics, 27, 225-238. https://doi.org/10.1017/S0022377800026556

Kennel, C. F., & Petschek, H. E. (1966). Limit on stably trapped particle fluxes. Journal of Geophysical Research, 71, 1-28. https://doi.org/10.1029/JZ071i001p00001

Kletzing, C. A., Kurth, W. S., Acuna, M., MacDowall, R. J., Torbert, R. B., Averkamp, T., et al. (2013). The Electric and Magnetic Field Instrument Suite and Integrated Science (EMFISIS) on RBSP. Space Science Reviews, 179(1-4), 127–181. https://doi.org/10.1007/s11214-013-9993-6

Koons, H. C. (1989). Observations of Large-Amplitude, Whistler Mode Wave Ducts in the Outer Plasmasphere. Journal of Geophysical Research, 94, 15,393-15,397.

https://doi.org/10.1029/JA094iA11p15393

Li, W., Thorne, R. M., Bortnik, J., Nishimura, Y., Angelopoulos, V., Chen, L., McFadden, J. P., & Bonnell, J. W. (2010). Global distributions of suprathermal electrons observed on THEMIS and potential mechanisms for access into the plasmasphere. Journal of Geophysical Research, 115, A00J10. https://doi.org/10.1029/2010JA015687

Li, W., Bortnik, J., Thorne, R. M., Nishimura, Y., Angelopoulos, V., & Chen, L. (2011). Modulation of whistler mode chorus waves: 2. Role of density variations. Journal of Geophysical Research, 116, A06206. https://doi.org/10.1029/2010JA016313

Loi, S. T., et al. (2015), Real-time imaging of density ducts between the plasmasphere and ionosphere, Geophys. Res. Lett., 42, 3707-3714. https://doi.org/10.1002/2015GL063699

Lu, Q., Ke, Y., Wang, X., Liu, K., Gao, X., Chen, L., &Wang, S. (2019). Two-dimensional gcPIC simulation of rising-tone chorus waves in a dipole magnetic field. Journal of Geophysical Research: Space Physics, 124, 4157–4167. https://doi.org/10.1029/2019JA026586

Means, J. D. (1972). Use of the three-dimensional covariance matrix in analyzing the polarization properties of plane waves. Journal of Geophysical Research, 77, 5551-5559. https://doi.org/10.1029/JA077i028p05551

Min, K., Liu, K., & Li, W. (2014). Signatures of electron Landau resonant interactions with chorus waves from THEMIS observations. Journal of Geophysical Research:

Space Physics, 119, 5551–5560. https://doi.org/10.1002/2014JA019903

Moullard, O., Masson, A., Laakso, H., Parrot, M., Décréau, P., Santolik, O., & Andre, M. (2002). Density modulated whistler mode emissions observed near the plasmapause. Geophysical Research Letters, 29, 36-1-36-4. https://doi.org/10.1029/2002GL015101

Mozer, F. S., Agapitov, O., Krasnoselskikh, V., Lejosne, S., Reeves, G. D., & Roth, I. (2014). Direct observation of radiation-belt electron acceleration from electron-volt energies to megavolts by nonlinear whistlers. Physical Review Letters, 113, 035001. https://doi.org/10.1103/PhysRevLett.113.035001

Omura, Y., Katoh, Y., & Summers, D. (2008). Theory and simulation of the generation of whistler-mode chorus. Journal of Geophysical Research, 113, 4223. https://doi.org/10.1029/2007JA012622

Reeves, G. D., Spence, H. E., Henderson, M. G., Morley, S. K., Friedel, R. H. W., Funsten, H. O., Baker, D. N., et al. (2013). Electron Acceleration in the Heart of the Van Allen Radiation Belts. Science, 341, 991-994. https://doi.org/10.1126/science.1237743

Scarabucci, R. R., & Smith, R. L. (1971). Study of Magnetospheric Field Oriented Irregularities—the Mode Theory of Bell-Shaped Ducts. Radio Scienc, 6, 65-86. https://doi.org/10.1029/RS006i001p00065

Scarf, F. L., Gurnett, D. A., & Kurth, W. S. (1979). Jupiter Plasma Wave Observations: An Initial Voyager 1 Overview. Science, 204(4396), 991-995. https://doi.org/10.1126/science.204.4396.991

Shprits, Y. Y., Menietti, J. D., Drozdov, A. Y., Horne, R. B., Woodfield, E. E., Groene, J. B., et al. Nature Communications, 9, 3131. https://doi.org/10.1038/s41467-018-05431-x

Smith, R. L., Helliwell, R. A., & Yabroff, I. W. (1960). A theory of trapping of whistlers in field-aligned columns of enhanced ionization. Journal of Geophysical Research, 65, 815-823. https://doi.org/10.1029/JZ065i003p00815

Smith, R. L., & Angerami, J. J. (1968). Magnetospheric properties deduced from OGO 1 observations of ducted and nonducted whistlers. Journal of Geophysical Research, 73, 1-20. https://doi.org/10.1029/JA073i001p00001

Sonwalkar, V. S. (2006). The influence of plasma density irregularities on whistler-mode wave propagation, in Geospace ElectromagneticWaves and Radiation, vol. 191, pp. 141-190, Springer, Berlin.

Sonwalkar, V. S., U. S. Inan, T. F. Bell, R. A. Helliwell, V. M. Chmyrev, Y. P. Sobolev, O. Y. Ovcharenko, and V. Selegej (1994), Simultaneous observations of VLF ground transmitter signals on the DE 1 and COSMOS 1809 satellites: Detection of a magnetospheric caustic and a duct, J. Geophys. Res., 99(A9), 17,511-17,522. https://doi.org/10.1029/94JA00866

Spence, H. E., Reeves, G. D., Baker, D. N., Blake, J. B., Bolton, M., Bourdarie, S., et al. (2013). Science Goals and Overview of the Radiation Belt Storm Probes (RBSP) Energetic Particle, Composition, and Thermal Plasma (ECT) Suite on NASA's Van Allen Probes Mission. Space Science Reviews, 179, 311–336. https://doi.org/10.1007/s11214-013-0007-5

Streltsov, A. V., Lampe, M., Manheimer, W., Ganguli, G., & Joyce, G. (2006). Whistler propagation in inhomogeneous plasma. Journal of Geophysical Research, 111, A03216. https://doi.org/10.1029/2005JA011357

Streltsov, A. V., Lampe, M., & Ganguli, G. (2007). Whistler propagation in nonsymmetrical density channels. Journal of Geophysical Research, 112, A06226. https://doi.org/10.1029/2006JA012093

Streltsov, A. V., & Bengtson, M. T. (2020). Observations and modeling of whistler mode waves in the magnetospheric density ducts. Journal of Geophysical Research: Space Physics, 125, e2020JA028398. https://doi.org/10.1029/2020JA028398

Summers, D., Omura, Y., Miyashita, Y., & Lee, D.-H. (2012), Nonlinear spatiotemporal evolution of whistler mode chorus waves in Earth's inner magnetosphere. Journal of Geophysical Research, 117, A09206, https://doi.org/10.1029/2012JA017842

Thorne, R. M., Ni, B., Tao, X., Horne, R. B., & Meredith, N. P. (2010). Scattering by chorus waves as the dominant cause of diffuse auroral precipitation. Nature, 467, 943-946. https://doi.org/10.1038/nature09467

Thorne, R. M., Li, W., Ni, B., Ma, Q., Bortnik, J., Chen, L., & Kanekal, S. G. (2013). Rapid local acceleration of relativistic radiation-belt electrons by magnetospheric chorus. Nature, 504, 411–414. https://doi.org/10.1038/nature12889

Tsurutani, B. T., & Smith, E. J. (1974). Postmidnight chorus: A substorm phenomenon. Journal of Geophysical Research, 79, 118–127.

https://doi.org/10.1029/Ja079i001p00118

Verkhoglyadova, O. P., Tsurutani, B.T., & Lakhina, G. S. (2010). Properties of obliquely propagating chorus. Journal of Geophysical Research, 115, A00F19. https://doi.org/10.1029/2009JA014809

Woodroffe, J. R., Streltsov, A. V., Vartanyan, A., & Milikh, G. M. (2013). Whistler propagation in ionospheric density ducts: Simulations and DEMETER observations. Journal of Geophysical Research: Space Physics, 118, 7011–7018. https://doi.org/10.1002/2013JA019445

Wygant, J. R., Bonnell, J. W., Goetz, K., Ergun, R. E., Mozer. F. S., Bale, S. D., et al. (2013). The Electric Field and Waves Instruments on the Radiation Belt Storm Probes Mission. Space Science Reviews, 179:183–220. https://doi.org/10.1007/s11214-013-0013-7

Xie, H. (2019). BO: A unified tool for plasma waves and instabilities analysis. Computer Physics Communications, 244, 343-371. https://doi.org/10.1016/j.cpc.2019.06.014

Acknowledgements

This research was funded by the NSFC grant 41774151, 41631071, 41527804, Key Research Program of Frontier Sciences CAS(QYZDJ-SSW-DQC010), USTC Research Funds of the Double First-Class Initiative, the Fundamental Research Funds for the Central Universities, Young Elite Scientists Sponsorship Program by CAST (2018QNRC001), and the Strategic Priority Research Program of Chinese Academy of Sciences Grant No. XDB41000000. WL would like to acknowledge the NSF grant

AGS-1847818 and the Alfred P. Sloan Research Fellowship FG-2018-10936. We also acknowledge the entire Van Allen Probes instrument team, and the data are available from the website: https://spdf.gsfc.nasa.gov/pub/data/rbsp/.

Figure captions:

Figure 1. Event overview observed by RBSP-A. (a) The schematic of the location where RBSP-A captured this event. (b) The electric field power spectral density in the Waves HFR channel (The f_{uh} is given by the white line, denoting the wave mode with the average frequency weighted by the power at each time). (c) Electron density. (d) The spectrogram of magnetic power $B_{w,s}$ and (e) electric power $E_{w,s}$, (f) θ_{Poyn}, and (g) wave normal angle (θ). Here, WNA (θ) represents the angle between the wave vector and background magnetic field, and θ_{Poyn} is the angle between the Poynting vector and background magnetic field. In each panel, the dotted and dashed lines in white or black represent 0.2 f_{ce} and 0.5 f_{ce}, respectively, where f_{ce} represents equatorial electron cyclotron frequency.

Figure 2. High-resolution whistler mode waves observed inside and out the duct. Two 6-sec burst segments: one is inside the density duct (left), and the other is outside the density duct (right). (a) The spectrogram of magnetic power $B_{w,b}$, (b) WNA θ, and (c) ratio Sz/S. S is the intensity of Poynting Flux and Sz is the parallel component.

Figure 3. Electron pitch angle distribution and calculated chorus wave growth rates. (a, b) The electron distributions as a function of pitch angle measured by the ECT during two events in Fig. 2. The electron distributions are indicated by the symbol "+", and the solid lines are the fitting curves. (c, d) The dispersion relations of unstable whistler mode waves for both events obtained from the linear model using input parameters listed in Table 2. The color bar denotes the linear growth rate. Here, 'k' is wave number. And 'λ' is electron inertial length, which is equal to c/ω_{pe}.

Figure 4. Electron density as a function of the perpendicular wave number of whistler mode waves. Panel a is a zoom-in view of shaded region in panel b. Different colors indicate whistler mode waves with different frequencies, such as 800 Hz, 900 Hz, 1000 Hz, and 1100 Hz. For each whistler mode, the red diamond and black star represent two critical densities n_0 and n_1 calculated based on the quasi-longitudinal dispersion relation. We have marked the density duct and ducted region by double-headed arrows.

Figure 5. The temporal profiles of magnetic amplitude for whistler modes waves. Panel a-d present whistler mode waves with f = 800 Hz, 900 Hz, 1000 Hz, and 1100 Hz, respectively. In each panel, the amplitude is calculated by integrating magnetic wave power using the survey-mode WFR data (black line), or continuous-burst waveform data (averaged with 1-second data; dots), and the shaded area is the ducted region for each whistler mode wave. Moreover, we plot the electron density n_e (red line), theoretical n_0 (dashed line), and observed n_0^* (dotted line), respectively. The specific frequency ranges are ~796-892Hz, ~892-1001Hz, 1001-1124Hz and 1124-1261Hz for f = 800 Hz, 900 Hz, 1000 Hz, and 1100 Hz, respectively.

TABLE 1. The fitting parameters for two electron distributions at observation sites: P_{in} is inside the duct, and P_{out} is outside the duct.

TABLE 2. The fitting parameters for two electron distributions at the magnetic equator: P_{in} is inside the duct, and P_{out} is outside the duct.

Figure1.

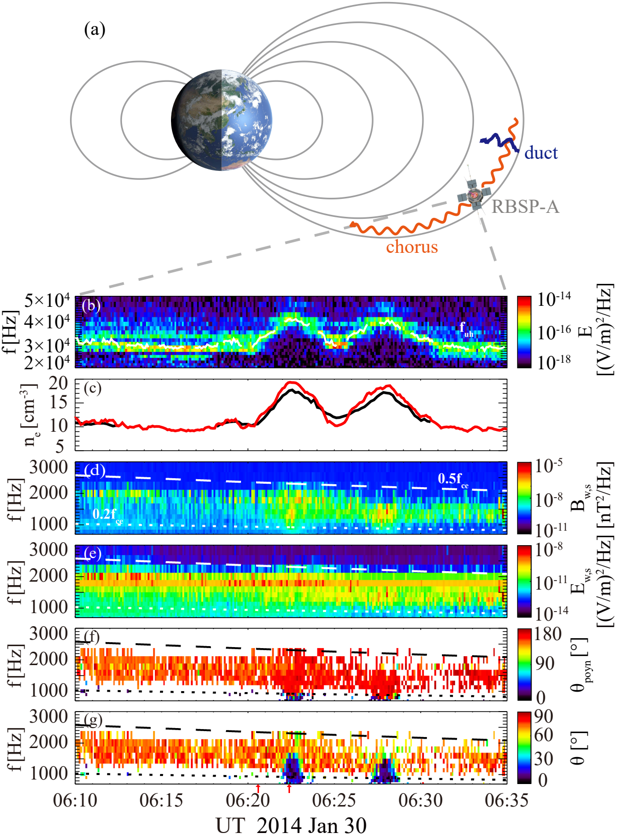

(a)
duct
RBSP-A
chorus
(b)
f [Hz]
5×10^4
4×10^4
3×10^4
2×10^4
f_uh
10^-14
10^-16
10^-18
E [(V/m)^2/Hz]
(c)
n_e [cm^-3]
20
15
10
5
(d)
f [Hz]
3000
2000
1000
0.5f_ce
0.2f_ce
10^-5
10^-8
10^-11
B_w,s [nT^2/Hz]
(e)
10^-8
10^-11
10^-14
E_w,s [(V/m)^2/Hz]
(f)
180
90
0
θ_poyn [°]
(g)
90
60
30
0
θ [°]
06:10
06:15
06:20
06:25
06:30
06:35
UT 2014 Jan 30

Figure2.

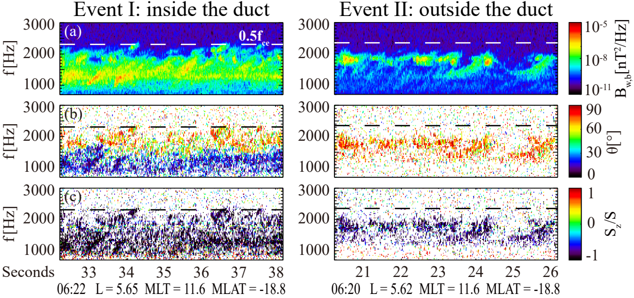

Event I: inside the duct
Event II: outside the duct
(a)
(b)
(c)
0.5f$_{ce}$
f [Hz]
3000
2000
1000
$B_{w,b}$[nT^2/Hz]
10^{-5}
10^{-8}
10^{-11}
θ[°]
90
60
30
0
S_z/S
1
0
-1
Seconds
33 34 35 36 37 38
21 22 23 24 25 26
06:22 L = 5.65 MLT = 11.6 MLAT = -18.8
06:20 L = 5.62 MLT = 11.6 MLAT = -18.8

Figure3.

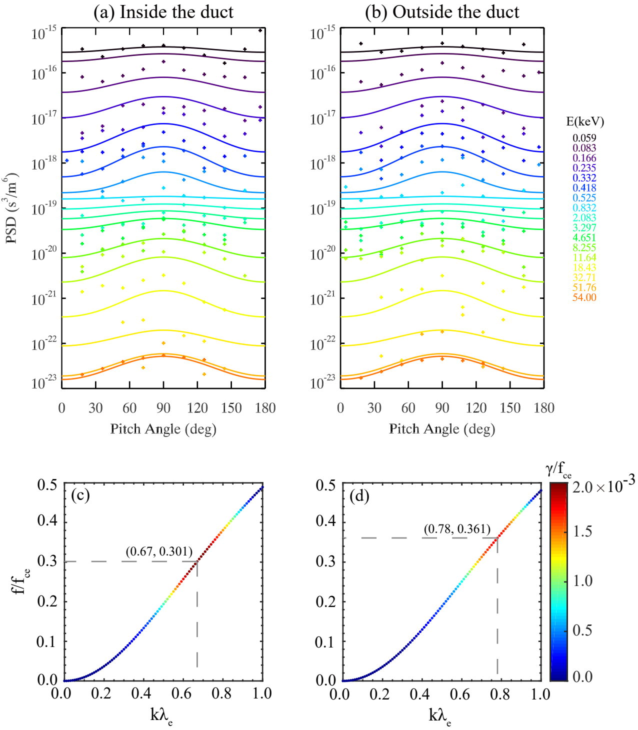
(a) Inside the duct
(b) Outside the duct
PSD (s^3/m^6)
Pitch Angle (deg)
E(keV)
0.059
0.083
0.166
0.235
0.332
0.418
0.525
0.832
2.083
3.297
4.651
8.255
11.64
18.43
32.71
51.76
54.00
(c)
(d)
(0.67, 0.301)
(0.78, 0.361)
f/f_ce
kλ_e
γ/f_ce
2.0×10^-3
1.5
1.0
0.5
0.0

Figure4.

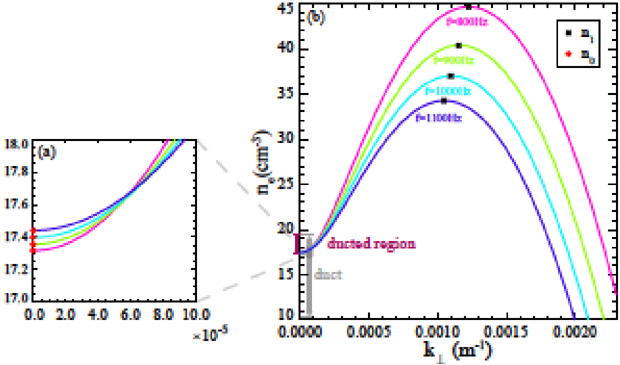

(a)
18.0
17.8
17.6
17.4
17.2
17.0
0.0 2.0 4.0 6.0 8.0 10.0
×10^-5
(b)
f=800Hz
f=900Hz
f=1000Hz
f=1100Hz
n1
n0
ducted region
duct
ne (cm^-3)
k⊥ (m^-1)
45
40
35
30
25
20
15
10
0.0000 0.0005 0.0010 0.0015 0.0020

Figure5.

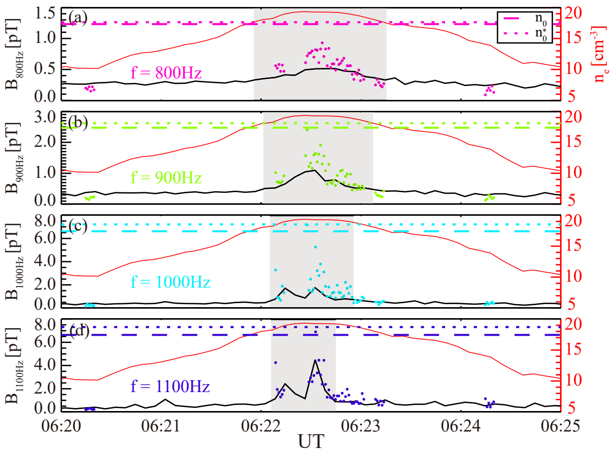

(a)
(b)
(c)
(d)
f = 800Hz
f = 900Hz
f = 1000Hz
f = 1100Hz
n_0
n_0^*
B_{800Hz} [pT]
B_{900Hz} [pT]
B_{1000Hz} [pT]
B_{1100Hz} [pT]
n_e [cm^{-3}]
06:20
06:21
06:22
06:23
06:24
06:25
UT

	B (nT)	n_c (cm^{-3})	$T_{\parallel c}, T_{\perp c}$ (eV)	n_w (cm^{-3})	$T_{\parallel w}$ (eV)	$T_{\perp w}/T_{\parallel w}$
P_{in}	262.3	18.7	5.0	0.52	52.4	1.32
P_{out}	267.1	9.6				
	n_{h1} (cm^{-3})	$T_{\parallel h1}$ (keV)	$T_{\perp h1}/T_{\parallel h1}$	n_{h2} (cm^{-3})	$T_{\parallel h2}$ (keV)	$T_{\perp h2}/T_{\parallel h2}$
P_{in} P_{out}	0.044	2.42	1.42	0.0027	12.42	1.37

	B_{eq} (nT)	n_c (cm^{-3})	$T_{\parallel c}, T_{\perp c}$ (eV)	n_w (cm^{-3})	$T_{\parallel w}$ (eV)	$T_{\perp w}/T_{\parallel w}$
P_{in}	164.8	18.7	5.0	0.63	52.4	1.62
P_{out}	167.9	9.6				
	n_{h1} (cm^{-3})	$T_{\parallel h1}$ (keV)	$T_{\perp h1}/T_{\parallel h1}$	n_{h2} (cm^{-3})	$T_{\parallel h2}$ (keV)	$T_{\perp h2}/T_{\parallel h2}$
P_{in} P_{out}	0.059	2.42	1.89	0.0035	12.42	1.76